

Ionization of argon by two-color laser pulses with coherent phase controlD. G. Arbó,^{1,*} C. Lemell,² S. Nagele,² N. Camus,³ L. Fechner,³ A. Krupp,³ T. Pfeifer,³ S. D. López,¹
R. Moshhammer,³ and J. Burgdörfer²¹*Institute for Astronomy and Space Physics, IAFE (CONICET-UBA), CC 67, Suc. 28 (1428) Buenos Aires, Argentina*²*Institute for Theoretical Physics, Vienna University of Technology, Wiedner Hauptstr. 8-10/E136, A-1040 Vienna, Austria, EU*³*Max-Planck-Institut für Kernphysik, Saupfercheckweg 1, 69117 Heidelberg, Germany, EU*

(Received 22 May 2015; published 3 August 2015)

We present a joint experimental and theoretical study of ionization of argon atoms by a linearly polarized two-color laser field ($\lambda_1 = 800$ nm, $\lambda_2 = 400$ nm). Changing the relative phase φ between the two colors, the forward-backward asymmetry of the doubly differential momentum distribution of emitted electrons can be controlled. We find excellent agreement between the measurements and the solution of the time-dependent Schrödinger equation in the single-active electron approximation. Surprisingly we also find good agreement between the quantum and classical calculations of electron momentum distributions generated by lasers at optical wavelengths.

DOI: [10.1103/PhysRevA.92.023402](https://doi.org/10.1103/PhysRevA.92.023402)

PACS number(s): 32.80.Rm, 32.80.Fb, 03.65.Sq

I. INTRODUCTION

Strong-field ionization by two-color laser fields with well-defined relative phase allows one to tune and to control the emission process giving rise to strong variations in the resulting energy and angular distribution of ionized electrons. Two-color pulses were used in previous investigations of above-threshold ionization (ATI) [1–3], controlled ionization [4–6], dichroism [7,8], and orientation of molecules [9]. Recently, they have also been applied to control interference fringes in the momentum distribution of electron emission [10–12] using the fundamental component and one of its harmonics.

The temporal shape of the field is determined by the intensities of the two components and their relative phase φ or, in other words, the time between the respective field maxima. Exploiting the influence of φ on physical processes involved in atomic ionization is often referred to as “coherent phase control” [1]. This coherence in the multicolor optical field is to be distinguished from the coherent response of the electronic wave packet giving rise to complex interference patterns in the momentum distributions of the ionized electron. The interference structures in photoelectron spectra can be identified as a diffraction pattern from a “time grating” composed of *intracycle* and *intercycle* interferences [13–16]. While the intercycle interferences give rise to the well-known ATI peaks, intracycle interferences lead to a modulation of the ATI spectrum offering information on the subcycle ionization dynamics. The interference process previously observed [10] and analyzed [14] for single-color fields is expected to be present for multicolor fields as well [11].

In the present study, we provide direct experimental evidence and a theoretical analysis for the control of the interference pattern as well as of the breaking of inversion symmetry by variation of the two-color phase φ of the optical field. We use a primary color in the near-infrared with $\lambda_1 \approx 800$ nm and a less intense frequency-doubled contribution in the visible blue at $\lambda_2 \approx 400$ nm. The experiment utilizes a reaction microscope (ReMi) which provides kinematically

complete data and allows us to resolve the complex pattern in the multidifferential photoemission cross section.

The prominent presence of intracycle and intercycle interferences strongly suggests that the emission process is dominated by quantum effects controlled by the wavelength of the optical fields. While in the midinfrared region ($\lambda \gtrsim 2000$ nm) emission spectra can be well reproduced by classical simulations [17–21], pronounced quantum effects are expected to be present for shorter wavelengths in the optical region used in the present work. However, upon averaging over the focal volume of the laser pulse, or more generally, upon washing out of the interference modulations (coarse graining), the results of quantum calculations may approach the classical limit of a classical trajectory Monte Carlo (CTMC) simulation. We will explore the surprisingly strong classical-quantum correspondence for the present system and discuss its implications.

The article is organized as follows. In Sec. II, we describe the experimental setup and summarize the calculation methods used: The nonperturbative solution of the time dependent Schrödinger equation (TDSE) in the single-active electron (SAE) approximation and its classical counterpart, the CTMC method. For comparison, we also show results for two popular perturbative solutions within the framework of the distorted-wave Born approximation (DWBA), the strong-field approximation (SFA) and the Coulomb-Volkov approximation (CVA). Our results are presented and discussed in Sec. III. Atomic units ($e = \hbar = m_e = 1$ a.u.) are used throughout unless stated otherwise.

II. METHODS**A. Experiment**

In the experiment, a ReMi [22] spectrometer is used to guide the charged fragments by electric and magnetic fields to their respective detectors. The time of flight and impact position of the particles on the detectors are recorded in coincidence allowing us to determine their three-dimensional momentum \vec{k} after ionization with high resolution. Taking the z coordinate as the spectrometer axis and x and y coordinates as the transverse directions, we achieve a momentum resolution of $\Delta k_x^{\text{electrons}} = \Delta k_y^{\text{electrons}} = 0.05$ a.u., $\Delta k_z^{\text{electrons}} =$

*diego@iafe.uba.ar

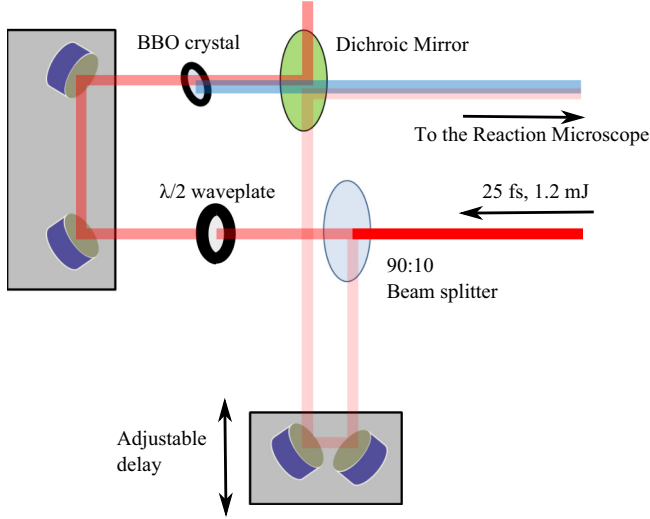


FIG. 1. (Color online) Schematic representation of the two-color Mach-Zehnder interferometer used to generate two-color laser pulses. See text for description.

0.01 a.u.; $\Delta k_x^{\text{ions}} = \Delta k_y^{\text{ions}} = 0.15$ a.u., $\Delta k_z^{\text{ions}} = 0.05$ a.u. (for a more detailed description of a ReMi setup and the necessary data evaluation procedure see, e.g., Refs. [22,23]). The laser pulses are created with a two-color Mach-Zehnder interferometer (Fig. 1). The red fundamental beam is the output of a commercial titanium:sapphire laser system with a central wavelength of $\lambda_1 = 790$ nm and a pulse duration of $\tau_1 = 25$ fs. It is split into two parts. One part remains unchanged, while the other part first passes a $\lambda/2$ wave plate and is then frequency doubled in a type I BBO crystal. Both beams are recombined behind a dichroic mirror and sent into the ReMi. The two fields are linearly polarized parallel to each other along the z axis. The intensities are estimated by comparing the experimental width of the ion longitudinal momentum distribution to the theoretical width obtained from the ADK formula [Eq. (10) in Ref. [24]] and, in addition, by comparing the double ionization yield as well as the Ar^{2+} momentum distribution to previously reported experiments [25,26]. Within 30% of confidence, the intensities are $I_1 = 2.4 \times 10^{14}$ W/cm² and $I_2 = 2.0 \times 10^{13}$ W/cm² for the red and blue components, respectively. The duration of the blue pulse is estimated to be $\tau_2 = 40$ fs.

In our simulations, we model this multicolor laser electric field by

$$F(t) = F_1 \sin^2\left(\frac{\pi t}{\tau_1}\right) \cos(\omega t + \varphi_{\text{CEP}}) + F_2 \sin^2\left(\frac{\pi t}{\tau_2}\right) \cos(2\omega t + \varphi_{\text{CEP}} + \varphi) \quad (1)$$

with φ_{CEP} the carrier-envelope phase (CEP). We use a \sin^2 envelope for both colors with pulse durations τ_i and amplitude $F_i \propto \sqrt{I_i}$, $i = 1, 2$. This envelope is a suitable representation of the experimental pulse shapes near the maxima where strong-field ionization takes place. In the simulation, we have varied the pulse duration from $\tau_2 = 2\tau_1$ (close to the experiment) to $\tau_2 = \tau_1$ and intensities from $I_1 = 1 \times 10^{14}$ W/cm² to 2.25×10^{14} W/cm² preserving the ratio $I_1/I_2 = 10$.

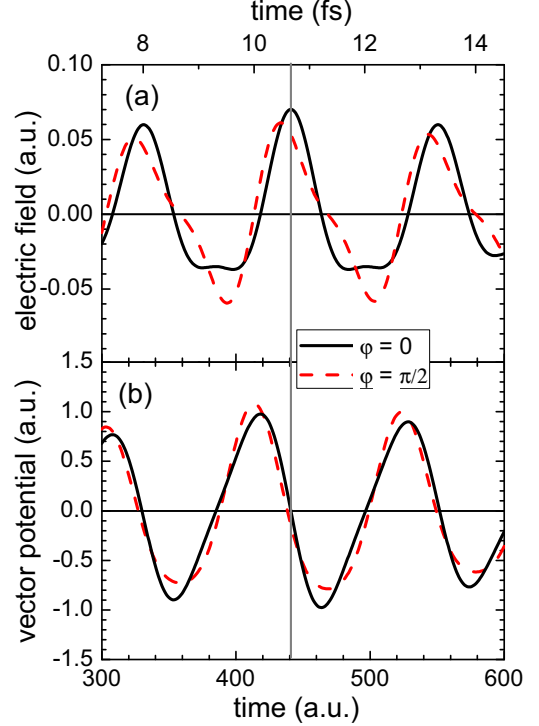


FIG. 2. (Color online) Laser electric fields and vector potentials of two-color laser pulses for the two-color phases $\varphi = 0$ (black solid line) and $\varphi = \pi/2$ (red dashed line). The intensities are $I_1 = 10^{14}$ W/cm² and $I_2 = 10^{13}$ W/cm².

The results turn out to be rather insensitive to the particular choice of τ_i .

In the experiment, the carrier envelope phase φ_{CEP} of the red pulse is not stabilized. However, the precise value of φ_{CEP} is of minor importance due to the long pulse duration. It does not induce any significant breaking of inversion symmetry and, thus, of the forward-backward asymmetry of the photoelectron emission. Instead, the phase φ [Eq. (1)] between the two colors serves as the control parameter for the degree to which inversion is broken as it results in variations of the effective vector potential and the electric field (Fig. 2). In the experiment, the “absolute value” of this two-color phase is not determined. However, its value φ is varied by an increment $\Delta\varphi$ through a controllable delay between the blue and red pulses. During the measurements, the length of the arm of the interferometer (Fig. 1) was changed continuously to cover the entire range of $\Delta\varphi \in [0, 2\pi]$. Accordingly,

$$\varphi = \varphi_0 + \Delta\varphi \quad (2)$$

with an unknown offset value φ_0 . We will show that the agreement between the quantum simulation and experimental results can be used to determine φ_0 in the experiment and, thus, the absolute value of φ .

The pulses are focused inside the ReMi by a spherical mirror ($f = 70$ mm) onto a low-density supersonic jet of argon (10^8 atoms/cm³). We assume a Gaussian profile of the laser beam with a focal radius of approximately 10 μm corresponding to a Rayleigh length of 400 μm for the red and 800 μm for the blue components. Changing the size of the gas

jet and its position with respect to the laser focus with the help of collimation slits, we did not detect any Gouy-phase effect.

In the simulations, we average the electron spectra over the experimental intensity distribution in the focal volume of the two-color laser pulse. Assuming a cylindrically symmetric beam with Gaussian intensity profile and maximum intensity I_0 , the volume with an intensity larger than I_i is proportional to [27]

$$V(I > I_i) \propto (2\beta + \beta^3/3 - 2 \arctan \beta) \quad (3)$$

with $\beta = \sqrt{I_0/I_i - 1}$. Averaging is done by performing calculations for many values of I_i keeping the ratio between the intensity maximum of the two fields constant. Due to the long computing times, intensity-averaged quantum simulations have been calculated only for selected values of φ .

B. Simulations

1. Solution of the time-dependent Schrödinger equation

We numerically solve the TDSE in the length gauge of the dipole approximation,

$$i \frac{\partial |\psi(t)\rangle}{\partial t} = \left\{ -\frac{\Delta}{2} + V(r) + zF(t) \right\} |\psi(t)\rangle, \quad (4)$$

in the SAE approximation. We employ the generalized pseudo-spectral method [28–30]. This method combines the discretization of the radial coordinate optimized for the Coulomb singularity with suitable quadrature methods allowing for stable long-time evolution using a split-operator representation of the time-evolution operator. Both the bound as well as the unbound parts of the wave function $|\psi(t)\rangle$ can be accurately represented. The atomic potential $V(r)$ is modeled as the sum of the asymptotic Coulomb potential, $V(r) = -1/r$, and a short-range potential accounting for the influence of the ionic core of Ar^+ . Its parameters are chosen to reproduce the ionization potential $I_p = 15.76$ eV and the energies of lower excited bound states [31]. Propagation of the wave function starts from the initial $3p$ ground state orbitals φ_{3p0} since the ionization from the $m = 0$ orbital, aligned along the laser polarization axis, strongly dominates over $m = -1, 1$ in the resulting spectrum. Due to the cylindrical symmetry of the atom in a linearly polarized laser field, the magnetic quantum number is conserved during the time evolution. Once the pulse is over, the wave function is projected onto eigenstates $|k, \ell\rangle$ of the field-free atomic Hamiltonian with positive eigenenergy $E = k^2/2$ and orbital quantum number ℓ in order to determine the transition amplitudes $t_{i \rightarrow k\ell}$.

The size of the computational box was chosen to be 1200 a.u. (~ 65 nm), which is considerably larger than the maximum quiver amplitude α of less than 20 a.u. in order to minimize unphysical reflections of the wave function at the boundary. Still, due to the long pulse duration employed in the experiment, parts of the electronic wave packet released at the maximum field with a momentum of $k \gtrsim 0.2$ a.u. may still reach the boundary of the box. Therefore, we have performed simulations with a total pulse duration of eight cycles of the primary color and 16 cycles of the frequency-doubled component, i.e., $\tau_1 = \tau_2$, and have checked that the pulse duration does not significantly affect the results of our simulations.

2. Classical-trajectory Monte Carlo method

Alternatively, we have modeled the experiment using a classical simulation. Our classical-trajectory Monte Carlo simulation has been described in detail elsewhere [32] and proceeds as follows: using the ADK tunneling rates for electrons with $m = 0$ and $m = \pm 1$ [33] the distribution of starting times t_0 for the propagation of classical trajectories following Newton's equation of motion is determined. The initial conditions for the longitudinal and perpendicular momenta at the tunnel exit are taken from Ref. [34]. The trajectory of emitted electrons in the combined laser and ionic fields is calculated using a standard fourth-order Runge-Kutta solver. The ionic potential $V(r)$ is calculated in the Hartree-Fock approximation [35]. Both the atomic potential and the external laser field are nonperturbatively included. All classical results shown in this paper have been averaged over the intensity profile of the laser beam using Eq. (3).

3. Distorted-wave approximations

The transition amplitude in the *post* form can be derived within the time-dependent first-order distorted wave approximation (DWBA) [36],

$$T_{if} = -i \int_{-\infty}^{+\infty} dt \langle \chi_f^-(t) | z F(t) | \phi_i(t) \rangle, \quad (5)$$

where $|\phi_i(t)\rangle$ is the initial atomic eigenstate with ionization energy I_p and $|\chi_f^-(t)\rangle$ is the final distorted wave function. The particular choice of $|\chi_f^-(t)\rangle$ reflects the distortion potential taken into account in the exit channel [37]. For example, in the SFA (first derived within the Keldysh-Faisal-Reiss theory [38–40]) $|\chi_f^-(t)\rangle$ is represented by Volkov states [41], which neglect the influence of the ionic core potential on the outgoing electron. Alternatively we have performed calculations in the Coulomb-Volkov approximation (CVA), which was first proposed by Jain and Tzoar [42] and extensively used for ionization by monochromatic low-intensity lasers [39,40,43–46]. In the CVA, $|\chi_f^-(t)\rangle$ contains both the phase of the Volkov state as well as the Coulomb continuum state of the field-free atom. For hydrogenic systems $|\chi_f^-(t)\rangle$ is analytically known [47,48] while it is numerically determined for atomic model potentials that include non-Coulombic short-ranged contributions.

III. RESULTS

A. Photoelectron spectra

One key observable is the photoelectron energy spectrum $P(E)$. In Fig. 3 we compare the experimental results with simulations for the two-color phase $\varphi = 0$ [Eq. (1)]. The experiment and the quantum simulation feature equidistant maxima due to the multiple absorption of photons at $E = n\hbar\omega - I_p - U_p$ (ATI maxima), with the ionization energy for Ar $I_p = 0.058$ a.u. = 15.76 eV, $\hbar\omega \approx 0.057$ a.u. = 1.55 eV the photon energy for the dominant color, and the ponderomotive energy $U_p = I_1/4\omega^2 + I_2/4(2\omega)^2 \approx I_1/4\omega^2$. We observe that the TDSE spectrum reproduces the experiment quite well within the entire energy range, except for the spikes at ~ 1 eV, which are most likely related to Freeman resonances [49,50] involving excited states in the Ar atom. Even though the results of CVA and SFA calculations show the multiphoton peaks,

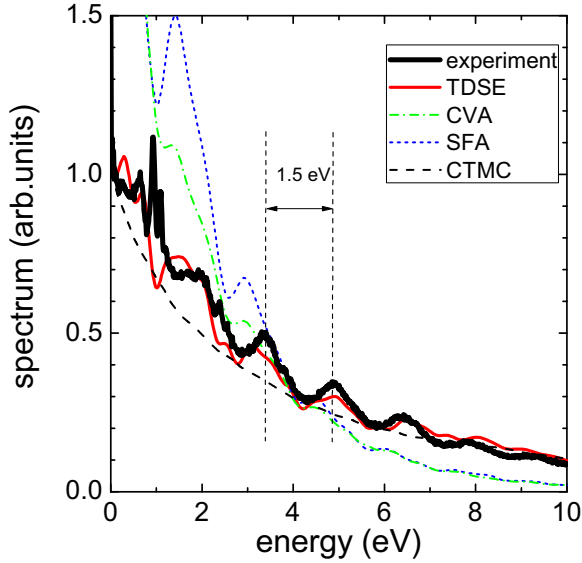


FIG. 3. (Color online) Experimental (black solid line) and simulated energy spectra for two-color phase $\varphi = 0$. TDSE (red thin solid line), CVA (green dot-dash line), SFA (blue dotted line), and CTMC (black dashed line). In the calculations, we have used the same laser intensities as in Fig. 2. To facilitate the comparison the curves have been normalized to agree with the TDSE data at around 4 eV.

the overall spectra differ substantially from the measured energy distribution; e.g., the average slope of CVA and SFA is much steeper than that of the measured spectrum. By contrast, while the CTMC spectrum, as expected, does not show any modulations resulting from the quantum nature of the photoionization process, its overall shape and slope reproduce the experimental spectrum remarkably well.

B. Momentum distributions

More detailed information on the strong-field photoemission process can be gained from doubly differential momentum distributions: distributions as a function of the longitudinal momentum k_z and the transverse momentum $k_\rho = \sqrt{k_x^2 + k_y^2}$, the momentum perpendicular to the polarization axis \hat{z} (because of azimuthal symmetry for linearly polarized fields, the coordinates k_x and k_y are equivalent). The phase-averaged experimental momentum distribution [Fig. 4(a)] is compared to corresponding simulations. For parallel momentum $k_z = -0.24$ a.u. the time of flight is equal to an integer multiple of the cyclotron period of the electrons in the magnetic field of the ReMi, and, thus, the transverse momentum is not resolved. The sharp double rings around 0.27 a.u. (marked with arrows) are the signatures of Freeman resonances, which are also visible in the energy spectrum at 1.1 eV in Fig. 3.

Near-threshold experimental and quantum angular distributions feature interference structures which have been observed for single-color ionization at 790 nm [50,51] and have been interpreted as generalized Ramsauer-Townsend diffraction patterns [52,53]. Their presence is rather insensitive to the two-color driving field and, consequently, to the average over φ . The number of angular nodes or, equivalently, the number of “rays” emanating from the origin ($\vec{k} = 0$) is controlled by

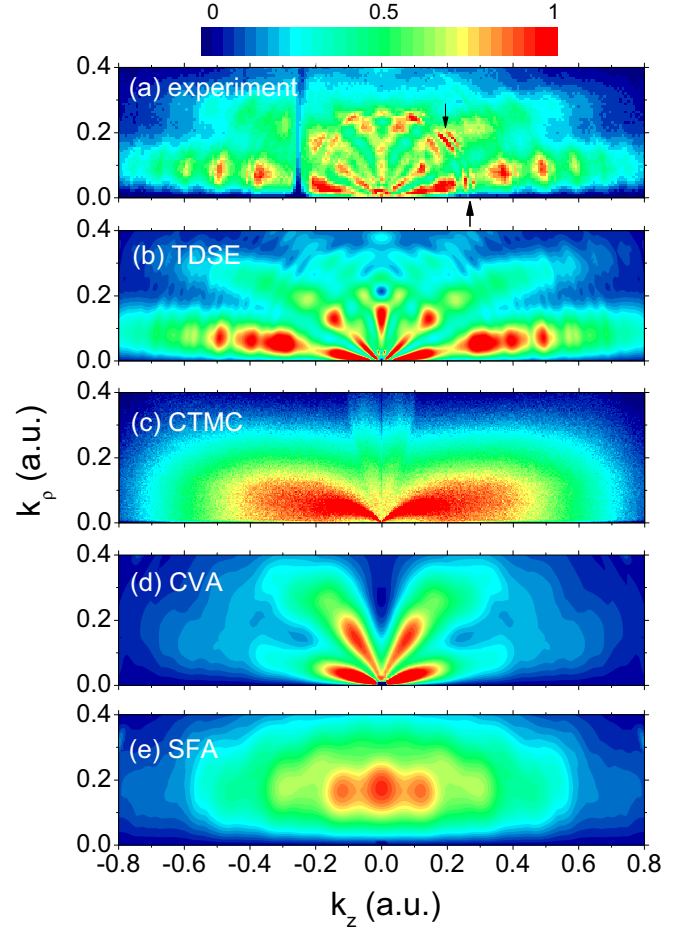


FIG. 4. (Color online) Electron momentum distributions for ionization of Ar by two-color laser pulses averaged over the phase φ on a linear color scale in arbitrary units. (a) Experiment, (b) TDSE, (c) CTMC, (d) CVA, and (e) SFA. All calculations take into account the intensity average over the focal volume. The arrows in (a) point to the double ring due to Freeman resonances (see text).

the dominant angular momentum of the emitted electrons $L(k) \approx \sqrt{2\alpha + \alpha^2 k^2}$ [53] with α the quiver amplitude. For the present laser parameters, we find a maximum value of $\alpha \approx 18$ independent of the two-color phase. Consequently, close to the threshold ($\vec{k} \approx 0$) the angular momentum becomes $L(0) \approx \sqrt{2\alpha} \approx 6$ in agreement with the nodal structure for small momenta. For larger momenta ($k = 0.25$ a.u.), traces of additional nodes appear in agreement with the estimate $L(k) \approx 7.5$. The phase- and intensity-averaged TDSE momentum distribution in Fig. 4(b) reproduces almost all features of the experimental data (except for the Freeman resonances): the “bouquet” shape structure as well as the ring structure stemming from the multiphoton absorption. Both distributions show similar extensions along the k_z and k_ρ axes.

The CTMC momentum distribution [Fig. 4(c)] neither shows the near-threshold Ramsauer-Townsend diffraction pattern nor ATI-ring structures as both arise from interference effects. However, the overall shape and average intensity pattern is rather well reproduced. By contrast, the distorted wave approximations, the CVA [Fig. 4(d)] and the SFA [Fig. 4(e)], reproduce some of the interference structures but

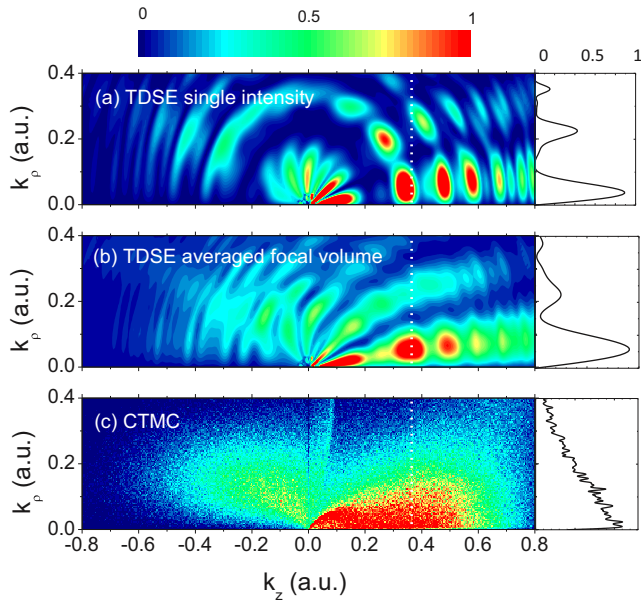


FIG. 5. (Color online) Momentum distributions of photoelectrons emitted from Ar calculated using (a) single intensity (no focal averaging) TDSE, (b) intensity-averaged TDSE, and (c) intensity-averaged CTMC simulations for the two-color phase $\varphi = 0$ on a linear color scale in arbitrary units. See Supplemental Material [54] for φ dependence. The right panels show a cut of the doubly differential distributions for $k_z = 0.37$, marked as a dotted line in the 2D plots.

fail to reproduce the overall intensity distribution. We therefore focus in the following on the φ dependence of the momentum distributions in the TDSE and CTMC simulations.

As an example for the degree of emission control obtained by the two-color phase φ , we show the momentum distributions resulting from the TDSE and CTMC simulations for $\varphi = 0$ in Fig. 5. The TDSE doubly differential momentum distributions for fixed intensities I_1 and I_2 without averaging

[Fig. 5(a)] and after intensity averaging over the focal volume [Fig. 5(b)] show, apart from the quantum interference structures, a strongly preferential emission in the forward direction (towards positive k_z). For this value of φ , the inversion symmetry is broken resulting in a pronounced forward-backward asymmetry with $P_{\text{ionization}}(k_\rho, k_z) \neq P_{\text{ionization}}(k_\rho, -k_z)$. Intensity averaging partly smears out the interference pattern [Fig. 5(b)]. The forward-backward asymmetry is remarkably well reproduced by the CTMC calculations [Fig. 5(c)]. Both the intensity-averaged TDSE and CTMC simulations feature a strongly focused forward emission and a weaker and broad structure at negative longitudinal momentum that extends from threshold up to $k_z \approx -0.4$ a.u. and $k_\rho \approx 0.2$.

Following a similar analysis for single-color infrared pulses [18,19,32], we explore the classical-quantum correspondence in the energy-angular momentum plane (Fig. 6). The single intensity TDSE distribution (left panel), the intensity-averaged TDSE distribution (center panel), and the CTMC distribution (right panel) closely resemble each other with the only noticeable difference being the missing interference pattern in the classical distribution. Prior to intensity averaging (left panel), the TDSE distribution features distinct maxima along horizontal lines at the ATI energies. The spots within a line are separated by $\Delta\ell \approx 2$ as expected from approximate dipole selection rules. In the CTMC distribution (right), we have marked two regions that display a pronounced dependence on φ (see animation in the Supplemental Material) [54]. The central maximum of the distribution (region 1) shifts its weight within the region between the two delimiting lines as φ is varied. Structure 2 is not found in single-color ionization at 800 nm and increases in intensity with increasing laser intensity of the blue-color field. It is a unique feature of two-color pulses appearing at almost constant low angular momentum ($\ell \approx 3$) and reaching beyond $2U_p$ for high energies suggesting an enhancement of the rescattering process driven by the two-color laser pulse.

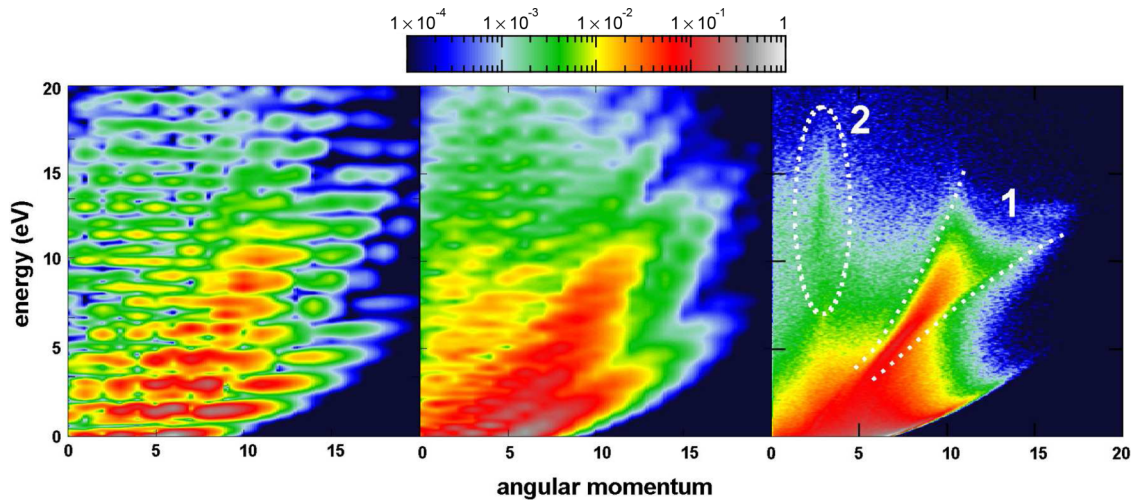


FIG. 6. (Color online) Electron energy versus angular momentum as calculated by TDSE and CTMC for $\varphi = 0$ on a logarithmic color scale covering four orders of magnitude. The TDSE results have been calculated without (left panel) and with intensity averaging (center panel). Depending on the two-color phase φ , the structures 1 and 2 marked in the CTMC distribution (right panel) appear differently pronounced (see animation in Supplemental Material) [54].

C. Inversion-symmetric observables

It is instructive to compare experiment and simulation for those physical observables that are insensitive to the broken inversion symmetry and are thus expected to be periodic in φ with period π . Examples are the total ionization yield P_{ion} or the mean escape energy of photoelectrons, $\langle E \rangle$. As can be seen from Fig. 7 both, P_{ion} and $\langle E \rangle$, show a φ -dependent variation with the expected π periodicity. The largest total photoemission probability is found for $\varphi = 0$ and $\varphi = \pi$, which can easily be understood by the increased maximum field strength for two pulses in phase, $F_{\text{max}}(\varphi = 0) = \sqrt{I_1 + I_2}$. Experiment and simulation show the π periodicity. The oscillation amplitude in the simulation is 10 times larger than measured in the experiment, the reason of which is not clear and needs further investigation. Intensity-averaged TDSE results again show almost perfect agreement with the classical simulation demonstrating the high degree of classical-quantum correspondence. Similar close agreement can be found for $\langle E \rangle$ in intensity-averaged simulations. Without intensity average,

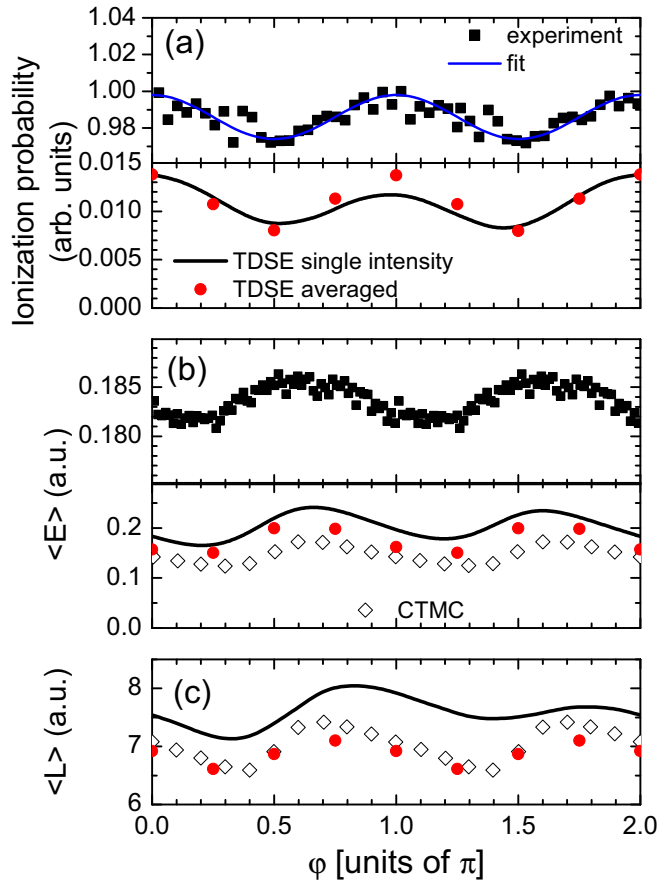


FIG. 7. (Color online) (a) Measured (upper panel) and calculated (lower panel) ionization yield as a function of the two-color phase. (b) Measured (upper panel) and calculated (lower panel) mean value of the electron energy $\langle E \rangle$ as a function of φ . (c) Calculated mean value of the electron angular momentum $\langle L \rangle$. TDSE calculations for a single intensity (black solid line) and averaged over the focal volume (red full data points). CTMC calculations with average over the focal volume (open diamonds). The experimental data have been phase-shifted to match the theoretical phase.

$\langle E \rangle$ is about 0.055 a.u. (1.5 eV) higher. Again, the oscillation amplitude in experiment is by a factor of 10 smaller than in the simulations.

Similarly the mean angular momentum $\langle L \rangle$ displays π -periodic oscillations. For the comparison between the quantum and the classical calculations we use the Langer connection formula [55], $L = \ell + 1/2$, between the angular momentum quantum number ℓ and the classical angular momentum L . Its expectation value oscillates around $\langle L \rangle \approx 7$. The agreement between classical and intensity-averaged quantum calculations is very good. In Fig. 7(a) (lower panel) we can observe that single-intensity TDSE ionization probability for $\varphi = \pi$ is about 18% lower than for $\varphi = 0$. This departure from the π periodicity can also be observed for the single-intensity TDSE mean energy and angular momentum in Fig. 7(b) (lower panel) and Fig. 7(c), respectively. This departure from a perfect π periodicity is a CEP effect due to the short duration of the pulse in the quantum simulations. Averaging over the focal volume restores the π periodicity making the TDSE calculations resemble the measurement more closely.

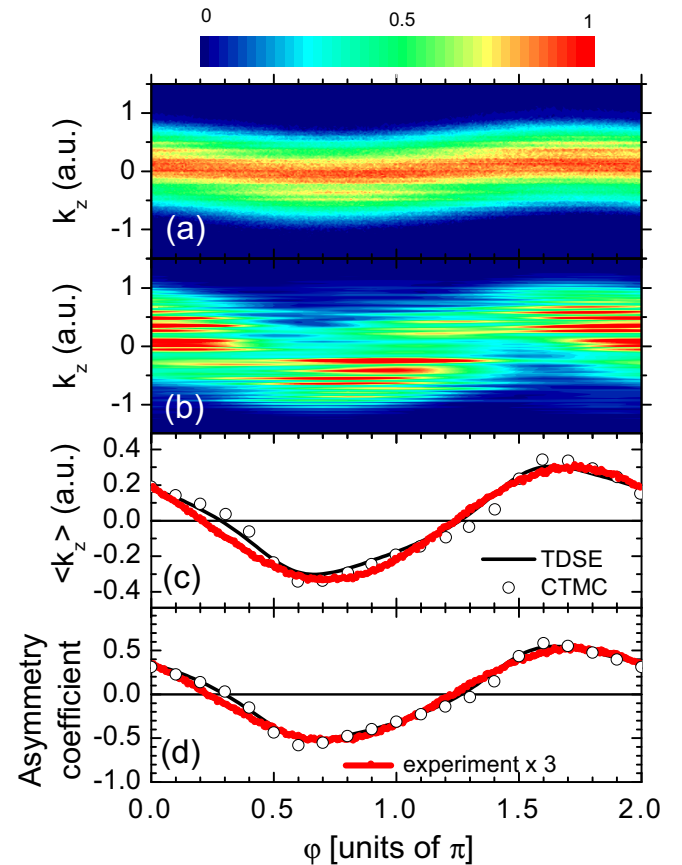


FIG. 8. (Color online) (a) Measured and (b) calculated longitudinal momentum distributions as a function of the two-color phase φ on a linear color scale in arbitrary units. Experimental (red thick solid line), TDSE (black thin solid line), and CTMC (open circles) mean values of the longitudinal momentum $\langle k_z \rangle$ in (c) and asymmetry parameter a in (d) as a function of φ . The TDSE calculations are for a single intensity only.

D. 2π -periodic observables

In order to quantify the breaking of inversion symmetry by the two-color laser pulse we focus now on observables O that are periodic by 2π rather than π , i.e., for which $\langle O \rangle(\pi + \varphi) \neq \langle O \rangle(\varphi)$. One obvious choice is the projection of the momentum distributions on the axis parallel to the laser polarization direction, dP/dk_z . The experimental data [Fig. 8(a)] and the TDSE calculations for a single intensity without average over the focal volume [Fig. 8(b)] clearly display oscillations with period 2π . Additionally, the calculation shows clear signatures of intercycle (ATI-like) interferences as horizontal stripes for φ between 0.5π and π near $k_z = -0.5$ a.u. and between 1.5π and 2π near $k_z = 0.5$ a.u., traces of which are barely visible in the experimental data due to intensity averaging. Likewise, the averaged longitudinal momentum, $\langle k_z \rangle$ in Fig. 8(c), is a 2π -periodic function which allows for an unambiguous determination of φ and thus of the offset φ_0 [Eq. (2)]. The present analysis underscores the precise control over the subcycle dynamics afforded by the two-color phase φ

of the $\omega - 2\omega$ field and its accurate description by the TDSE solution within the SAE framework.

Another measure for the forward-backward asymmetry is the asymmetry parameter a defined as

$$a(\varphi) = \frac{P_{\text{ionization}}(+)-P_{\text{ionization}}(-)}{P_{\text{ionization}}(+)+P_{\text{ionization}}(-)}, \quad (6)$$

where $P_{\text{ion}}(+)=2\pi\int_0^\infty dk_z\int_0^\infty dk_\rho k_\rho|T_{if}|^2$ and $P_{\text{ion}}(-)=2\pi\int_{-\infty}^0 dk_z\int_0^\infty dk_\rho k_\rho|T_{if}|^2$ are the total emission probabilities in forward and backward directions, respectively. We note that for $a(\varphi)$ and $\langle k_z \rangle(\varphi)$ quantum and classical simulations agree even without intensity averaging.

E. Comparison of the momentum distribution

After having determined the phase offset φ_0 and thus the absolute value of the $\omega - 2\omega$ control phase φ [Eq. (2)], we can now directly compare the measured and calculated TDSE momentum distributions for different phases (Fig. 9). The

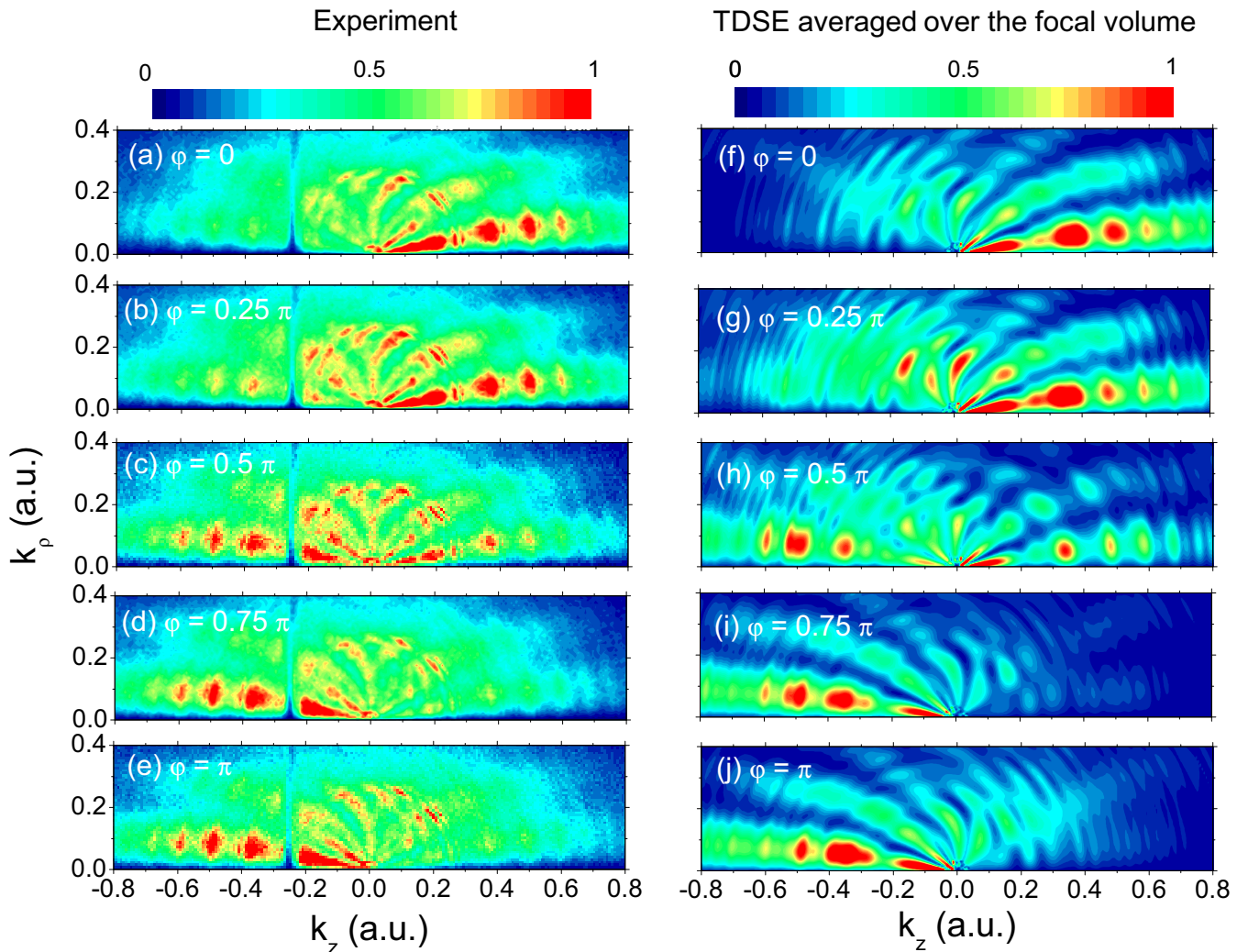


FIG. 9. (Color online) Measured (left column) and calculated (right column) electron momentum distributions for fixed two-color phases: $\varphi = 0$ on a linear color scale in arbitrary units (a) and (f), 0.25π (b) and (g), 0.5π (c) and (h), 0.75π (d) and (i), and π (e) and (j). The TDSE calculations have been performed including intensity averaging over the focal volume.

overall agreement of the main features of the experimental momentum distributions (left column of Fig. 9) and the results of the intensity-averaged TDSE calculations (right column of Fig. 9) is striking: washed-out ATI rings with maximum intensity for near forward or backward direction as well as the angular nodes from the Ramsauer-Townsend diffraction patterns are accurately reproduced even with similar fringe visibility. Although the qualitative features are also found in the single-intensity TDSE calculation [Fig. 5(a)], the quantitative agreement with the experiment is much enhanced when accounting for the experimental intensity distribution in the laser focus. We find that the direction of emission strongly depends on φ . We observe the dominant emission in the forward direction for $\varphi = 0$ [Figs. 9(a) and 9(f)]. As expected, the distributions for $\varphi = \pi$ are the mirror images to the distributions at $\varphi = 0$ [Figs. 9(e) and 9(j)] with no significant CEP effects in both experiment and calculations. As φ changes from $\varphi = 0$ to $\varphi = \pi$ the momentum distributions shift from the forward to the backward direction. In the case of $\varphi = 0.25\pi$ [Figs. 9(b) and 9(g)] visual inspection of the maxima of the distributions would suggest a strong preference in forward direction while the mean values $\langle k_z \rangle(\varphi)$ and $a(\varphi)$ averaged over all transverse momenta are, in fact, close to zero.

IV. CONCLUSIONS

We have presented a combined experimental and theoretical analysis of single ionization of argon atoms interacting with linearly polarized two-color laser fields ($\lambda_1 = 800$ nm, $\lambda_2 = 400$ nm). Electron momentum distributions have been recorded with a reaction microscope and compared to different theoretical model-calculation spectra. After focal averaging, very good agreement was achieved between experimental and simulated results. The level of agreement allows for the determination of the absolute phase of the two-color phase φ between the ω and

2ω fields unambiguously. The electron momentum distribution as well as the forward-backward asymmetry parameter is sensitively dependent on φ , controlling the degree to which the two-color radiation field breaks the inversion symmetry. This φ dependence is to be distinguished from the effect of the carrier-envelope phase φ_{CEP} , which is responsible for the violation of inversion symmetry for short single-color pulses. φ_{CEP} plays no significant role for the longer pulses used here ($\tau \approx 30$ fs) and remains undetermined in the experiment.

The present analysis illustrates the remarkable degree of quantum-classical correspondence for the strong-field ionization by a two-color field with (near) optical frequencies. We find surprisingly good agreement between CTMC and TDSE simulations, in particular when quantum-interference oscillations are (partly) washed out by focal averaging. These observations lend support to the recent suggestion for single-color pulses [56,57] that inclusion of semiclassical interference phases into a CTMC simulation should lead to closer agreement with TDSE simulations than frequently employed approximate quantum calculations based on distorted-wave Born approximations.

ACKNOWLEDGMENTS

This work was supported by CONICET PIP0386, Austria-Argentina collaboration AU/12/02 and PICT2010-1084 of ANPCyT (Argentina), the University of Buenos Aires (UBA-CyT617), the Austrian Science Fund (FWF) special research programs SFB-041 (ViCoM) and SFB-049 (NextLite), doctoral programme DK-W1243 (Solid4Fun), and project P21141-N16, the European COST Action CM1204 (XLIC), and a WTZ project of the OeAD (AR 03/2013). The computational results presented have been achieved in part using the Vienna Scientific Cluster (VSC).

-
- [1] F. Ehlotzky, *Phys. Rep.* **345**, 175 (2001).
 - [2] D. W. Schumacher, F. Weihe, H. G. Muller, and P. H. Bucksbaum, *Phys. Rev. Lett.* **73**, 1344 (1994).
 - [3] H. G. Muller, P. H. Bucksbaum, D. W. Schumacher, and A. Zavriyev, *J. Phys. B* **23**, 2761 (1990).
 - [4] M. R. Thompson, M. K. Thomas, P. F. Taday, J. H. Posthumus, A. J. Langley, L. J. Frasinski, and K. Codling, *J. Phys. B* **30**, 5755 (1997).
 - [5] B. Sheehy, B. Walker, and L. F. DiMauro, *Phys. Rev. Lett.* **74**, 4799 (1995).
 - [6] H. Ohmura, T. Nakanaga, and M. Tachiya, *Phys. Rev. Lett.* **92**, 113002 (2004).
 - [7] M. Fifrig, A. Cionga, and F. Ehlotzky, *Eur. Phys. J. D* **23**, 333 (2003).
 - [8] A. Cionga, M. Fifrig, and F. Ehlotzky, *J. Mod. Opt.* **50**, 615 (2003).
 - [9] S. De, I. Znakovskaya, D. Ray, F. Anis, N. G. Johnson, I. A. Bocharova, M. Magrakvelidze, B. D. Esry, C. L. Cocke, I. V. Litvinyuk, and M. F. Kling, *Phys. Rev. Lett.* **103**, 153002 (2009).
 - [10] X. Xie, S. Roither, D. Kartashov, E. Persson, D. G. Arbó, L. L. Zhang, S. Gräfe, M. S. Schöffler, J. Burgdörfer, A. Baltuška, and M. Kitzler, *Phys. Rev. Lett.* **108**, 193004 (2012).
 - [11] D. G. Arbó, S. Nagele, X.-M. Tong, X. Xie, M. Kitzler, and J. Burgdörfer, *Phys. Rev. A* **89**, 043414 (2014).
 - [12] D. G. Arbó, *J. Phys. B* **47**, 204008 (2014).
 - [13] S. Bivona, G. Bonanno, R. Burlon, D. Gurrera, and C. Leone, *Phys. Rev. A* **77**, 051404 (2008); S. Bivona, G. Bonanno, R. Burlon, and C. Leone, *ibid.* **79**, 035403 (2009).
 - [14] D. G. Arbó, K. L. Ishikawa, K. Schiessl, E. Persson, and J. Burgdörfer, *Phys. Rev. A* **81**, 021403(R) (2010).
 - [15] D. G. Arbó, K. L. Ishikawa, K. Schiessl, E. Persson, and J. Burgdörfer, *Phys. Rev. A* **82**, 043426 (2010).
 - [16] D. G. Arbó, K. L. Ishikawa, E. Persson, and J. Burgdörfer, *Nucl. Instrum. Meth. Res. B* **279**, 24 (2012).
 - [17] W. Quan, Z. Lin, M. Wu, H. Kang, H. Liu, X. Liu, J. Chen, J. Liu, X. T. He, S. G. Chen, H. Xiong, L. Guo, H. Xu, Y. Fu, Y. Cheng, and Z. Z. Xu, *Phys. Rev. Lett.* **103**, 093001 (2009).

- [18] C. Lemell, K. I. Dimitriou, X.-M. Tong, S. Nagele, D. V. Kartashov, J. Burgdörfer, and S. Gräfe, *Phys. Rev. A* **85**, 011403(R) (2012).
- [19] C. Lemell, J. Burgdörfer, S. Gräfe, K. I. Dimitriou, D. G. Arbó, and X.-M. Tong, *Phys. Rev. A* **87**, 013421 (2013).
- [20] A. Kästner, U. Saalman, and J. M. Rost, *J. Phys. B* **45**, 074011 (2012).
- [21] A. Kästner, U. Saalman, and J. M. Rost, *Phys. Rev. Lett.* **108**, 033201 (2012).
- [22] V. de Jesus, A. Rudenko, B. Feuerstein, K. Zrost, C. Schröter, R. Moshhammer, and J. Ullrich, *J. Elec. Spect. Rel. Phen.* **141**, 127 (2004).
- [23] J. Ullrich, R. Moshhammer, A. Dorn, R. Dörner, L. P. H. Schmidt, and H. Schmidt-Böcking, *Rep. Prog. Phys.* **66**, 1463 (2003).
- [24] N. B. Delone and V. P. Krainov, *Phys.-Uspek.* **41**, 469 (1998).
- [25] S. Larochelle, A. Talebpour, and S. L. Chin, *J. Phys. B* **31**, 1201 (1998).
- [26] A. Rudenko, Th. Ergler, K. Zrost, B. Feuerstein, V. L. B. de Jesus, C. D. Schröter, R. Moshhammer, and J. Ullrich, *Phys. Rev. A* **78**, 015403 (2008).
- [27] S. Augst, D. D. Meyerhofer, D. Strickland, and S. L. Chin, *J. Opt. Soc. Am. B* **8**, 858 (1991).
- [28] X.-M. Tong and S. I. Chu, *Chem. Phys.* **217**, 119 (1997).
- [29] X.-M. Tong and Shih-I. Chu, *Phys. Rev. A* **61**, 031401(R) (2000).
- [30] X.-M. Tong and C. D. Lin, *J. Phys. B* **38**, 2593 (2005).
- [31] H. G. Muller and F. C. Kooiman, *Phys. Rev. Lett.* **81**, 1207 (1998).
- [32] B. Wolter, C. Lemell, M. Baudisch, M. G. Pullen, X.-M. Tong, M. Hemmer, A. Senftleben, C. D. Schröter, J. Ullrich, R. Moshhammer, J. Biegert, and J. Burgdörfer, *Phys. Rev. A* **90**, 063424 (2014).
- [33] M. V. Ammosov, N. B. Delone, and V. P. Krainov, *Zh. Eksp. Teor. Fiz.* **91**, 2008 (1986) [*Sov. Phys. JETP* **64**, 1191 (1986)].
- [34] N. B. Delone and V. P. Krainov, *J. Opt. Soc. Am. B* **8**, 1207 (1991).
- [35] C. Froese-Fischer, *Comp. Phys. Comm.* **43**, 355 (1987).
- [36] D. P. Dewangan and J. Eichler, *Phys. Rep.* **247**, 59 (1994).
- [37] D. G. Arbó, J. E. Miraglia, M. S. Gravielle, K. Schiessl, E. Persson, and J. Burgdörfer, *Phys. Rev. A* **77**, 013401 (2008).
- [38] V. Keldysh, *Zh. Eksp. Theo. Fiz.* **47**, 1945 (1964) [*Sov. Phys. JETP* **20**, 1307 (1965)].
- [39] F. H. M. Faisal, *J. Phys. B* **6**, L89 (1973).
- [40] H. R. Reiss, *Phys. Rev. A* **22**, 1786 (1980).
- [41] D. M. Volkov, *Z. Phys.* **94**, 250 (1935).
- [42] M. Jain and N. Tzoar, *Phys. Rev. A* **18**, 538 (1978).
- [43] S. Basile, F. Trombetta, G. Ferrante, R. Burlon, and C. Leone, *Phys. Rev. A* **37**, 1050 (1988).
- [44] D. B. Milosevic and F. Ehlotzky, *Phys. Rev. A* **58**, 3124 (1998).
- [45] J. Z. Kaminski, A. Jaron, and F. Ehlotzky, *Phys. Rev. A* **53**, 1756 (1996).
- [46] C. Figueira de Morisson Faria, H. Schomerus, and W. Becker, *Phys. Rev. A* **66**, 043413 (2002).
- [47] P. A. Macri, J. E. Miraglia, and M. S. Gravielle, *J. Opt. Soc. Am. B* **20**, 1801 (2003).
- [48] V. D. Rodriguez, E. Cormier, and R. Gayet, *Phys. Rev. A* **69**, 053402 (2004); V. D. Rodriguez, P. Macri, and D. G. Arbó, *Nucl. Instrum. Meth. Res. B* **267**, 334 (2009).
- [49] R. R. Freeman, P. H. Bucksbaum, H. Milchberg, S. Darack, D. Schumacher, and M. E. Geusic, *Phys. Rev. Lett.* **59**, 1092 (1987).
- [50] C. M. Maharjan, A. S. Alnaser, I. Litvinyuk, P. Ranitovic, and C. L. Cocke, *J. Phys. B* **39**, 1955 (2006).
- [51] A. Rudenko, K. Zrost, C. D. Schröter, V. L. B. de Jesus, B. Feuerstein, R. Moshhammer, and J. Ullrich, *J. Phys. B* **37**, L407 (2004).
- [52] D. G. Arbó, S. Yoshida, E. Persson, K. I. Dimitriou, and J. Burgdörfer, *Phys. Rev. Lett.* **96**, 143003 (2006).
- [53] D. G. Arbó, K. I. Dimitriou, E. Persson, and J. Burgdörfer, *Phys. Rev. A* **78**, 013406 (2008).
- [54] See Supplemental Material at <http://link.aps.org/supplemental/10.1103/PhysRevA.92.023402> for animation of φ -dependent electron distributions.
- [55] R. E. Langer, *Phys. Rev.* **51**, 669 (1937).
- [56] M. Li, J.-W. Geng, H. Liu, Y. Deng, C. Wu, L.-Y. Peng, Q. Gong, and Y. Liu, *Phys. Rev. Lett.* **112**, 113002 (2014).
- [57] N. I. Shvetsov-Shilovski, L. B. Madsen, E. Räsänen, J. Burgdörfer, and K. Tókési, *J. Phys.: Conf. Ser.* (to be published).